Commun. Comput. Phys.
doi: 10.4208/cicp.OA-2016-0035

Vol. **22**, No. 1, pp. 39-63
July 2017

A Unified Momentum Equation Approach for Computing Flow-Induced Stresses in Structures with Arbitrarily-Shaped Stationary Boundaries

Haram Yeo and Hyungson Ki*

Department of Mechanical Engineering, Ulsan National Institute of Science and Technology (UNIST), 50 UNIST-gil, Ulsan 44919, South Korea.

Communicated by Lianjie Huang

Received 2 March 2016; Accepted (in revised version) 5 September 2016

Abstract. This article presents a novel monolithic numerical method for computing flow-induced stresses for problems involving arbitrarily-shaped stationary boundaries. A unified momentum equation for a continuum consisting of both fluids and solids is derived in terms of velocity by hybridizing the momentum equations of incompressible fluids and linear elastic solids. Discontinuities at the interface are smeared over a finite thickness around the interface using the signed distance function, and the resulting momentum equation implicitly takes care of the interfacial conditions without using a body-fitted grid. A finite volume approach is employed to discretize the obtained governing equations on a Cartesian grid. For validation purposes, this method has been applied to three examples, lid-driven cavity flow in a square cavity, lid-driven cavity flow in a circular cavity, and flow over a cylinder, where velocity and stress fields are simultaneously obtained for both fluids and structures. The simulation results agree well with the results found in the literature and the results obtained by COMSOL Multiphysics®.

AMS subject classifications: 74A10, 76M12

Key words: Flow induced stress, unified momentum equation, monolithic approach, smeared interface, stationary boundary.

1 Introduction

Flow induced stress is ubiquitous in nature and is at the core of many important engineering problems, such as vascular flows [1,2], flows around wind turbine blades [3], and ship in water [4]. Due to its complexity, the numerical approach is deemed the most practical, and therefore there have been a great deal of interest in making efficient and capable

*Corresponding author. *Email addresses:* hr7680@unist.ac.kr (H. Yeo), hski@unist.ac.kr (H. Ki)

numerical algorithms [5]. Although it is important to compute both fluid flow and stress development in a structure in many cases, a proper coupling of the fluid and the structure is challenging due to their dissimilar governing equations and physical behavior. Furthermore, complex structure geometry makes the problem even more difficult.

Generally, there are two approaches for the coupling of flow and structure: partitioned approach and monolithic approach. In the partitioned approach, different phases are solved separately using different solvers and the information is transferred across the interface enforcing the interface conditions [6, 7]. This approach has been traditionally preferred because existing codes for both phases can be used, but the numerical instabilities may occur due to the added-mass effect [8]. A strongly-coupled scheme can remedy these problems with extra iterations, which however is computationally expensive [9]. On the other hand, the monolithic approach solves the flow-structure system with a single algorithm. Although the development of a well-conditioned system is difficult due to the entirely different properties of fluids and solids, this approach is more robust than the partitioned approach. Accordingly, many monolithic methods have been developed with various coupling strategies. For example, Hübner et al. developed a monolithic method based on the space-time finite element method, where a weighted residual formulation was used for the coupling [10]. Heil proposed a monolithic method for fluid-structure interaction problems by using Newton's method [11]. He showed that block-triangular approximations of the Jacobian matrix, which was obtained by neglecting selected fluid-structure interaction blocks, provide good preconditioners for the solution of the linear systems with GMRES. Ryzhakov et al. [12] derived a displacement-based monolithic formulation by using global pressure condensation, where a matrix-free technique was used for efficiency and a free surface flow with a flexible structure was solved. Franci et al. [13] introduced a unified formulation based on a mixed velocity-pressure formulation to simulate Newtonian fluids and quasi-incompressible hypoelastic structures where the finite element method was used for structures and the particle finite element method was used for fluids.

Another important issue is how to treat complex geometries of structures. One approach is the use of a body-fitted grid where grid is aligned with interface. Then, interfacial conditions can be directly enforced and obtaining the interaction between fluid and structure is straightforward. However, the grid generation and discretization procedure can become complicated. A more efficient approach is the use of a non-body-fitted grid, such as the immersed boundary method and the fictitious domain method. The immersed boundary method which was originally devised by Peskin [14, 15] to compute blood flow in heart valves, expresses an immersed structure as a momentum forcing term. This method is suited for fiber-like structures and was effectively applied to many problems. However, there is a difficulty in applying the method to rigid structures and various numerical methods have been proposed. For example, in the direct forcing method, the representation of a structure is simplified by imposing the no-slip condition at the interface [16, 17]. The cut-cell method is proposed to satisfy the con-

servation law near the immersed structure, where the cells cut by an interface are reshaped to align with the geometry [18, 19]. In the ghost-cell method, the ghost cell is introduced inside the structure and boundary conditions are implicitly included in the interpolation scheme [20, 21]. In these methods for rigid structures, the flows with complex interfaces are efficiently handled on a non-body-fitted grid but stress fields inside the structures are not considered. Also, the immersed boundary method has been improved to consider more general structures and analyze the stress field more accurately. Zhang et al. [22] developed the immersed finite element method where a finite element formulation is applied to both fluids and structures in order to solve the structure region accurately and the interaction between fluids and structures is achieved with the reproducing kernel particle method (RKPM). Gil et al. [23] proposed the immersed structural potential method where the structure is represented as a strain energy functional. In this method, the fluid-structure interaction force field obtained from the strain energy functional is put in the Navier-Stokes equation as a source term. Another non-body-fitted method is the fictitious domain method. In the fictitious domain method, Glowinski et al. [24] introduced the Lagrange multiplier to achieve a fluid-structure coupling and Baaijens [25] improved the method by combining with the mortar element method to simulate slender bodies. For more general structures, Yu [26] enhanced the distributed-Lagrange-multiplier/fictitious-domain formulation. He used continuum equations instead of Newton's equations of motion and applied the method to Newtonian fluids and neo-Hookean elastic structures. Also, the lattice Boltzmann method has been drawing attention due to its simplicity of using a regular lattice. The method was developed to effectively handle the complex fluid problems such as multiphase flows [27]. In addition, the lattice Boltzmann method was applied to simulate the flows around obstacles. For example, Ladd et al. simulated the particulate flows where the bounce back rule is used to enforce the no-slip condition at the interface [28, 29].

This paper proposes a novel monolithic algorithm for computing stress fields in a structure as well as velocity fields in a fluid flow, where fluid-structure boundaries are stationary. Our approach is to consider a fluid-structure system as a single continuum, where the momentum equations for fluids and structures are hybridized inside the smeared boundary region by actually mixing the momentum equations using the level set function. Because of the way the momentum equation is formulated, a tight coupling of the momentum equations can be achieved, and arbitrarily-shaped boundaries can be easily taken care of. The resulting unified momentum equation can be solved by a proper numerical method for computational fluid dynamics. In this study, the SIMPLE algorithm (Semi-Implicit Method for Pressure Linked Equations) has been employed to solve three benchmark problems (lid-driven cavity flow in a square cavity, lid-driven cavity flow in a circular cavity, and flow over a cylinder) based on incompressible flows and linear elastics for test purposes. The simulation results agreed well with the results found in the literature and the results obtained by COMSOL Multiphysics®. It is believed that the ideas presented in this study can be extended to other types of fluids and solids.

2 Mathematical model

In this section, the governing equations for fluids and solids will be examined, and the unified momentum equation will be derived.

2.1 Fluid equation

The governing equations for incompressible Newtonian fluids consist of the Navier-Stokes equation and the continuity equation as follows:

$$\frac{D(\rho\mathbf{u})}{Dt} = \nabla\cdot\boldsymbol{\sigma}_f + \mathbf{f}, \tag{2.1}$$

$$\nabla\cdot\mathbf{u} = 0. \tag{2.2}$$

Here, ρ is density, $\mathbf{u}$ is the velocity vector, $\mathbf{f}$ is the body force, and the stress tensor $\boldsymbol{\sigma}_f$ is written as

$$\boldsymbol{\sigma}_f = -p\mathbf{I} + 2\eta\mathbf{R}, \tag{2.3}$$

where p is the pressure, η is the viscosity, and $\mathbf{R}$ is the rate of strain tensor,

$$\mathbf{R} = \frac{1}{2}\left(\nabla\mathbf{u} + \nabla\mathbf{u}^T\right). \tag{2.4}$$

From Eqs. (2.1), (2.3), and (2.4), the following momentum equation for fluids is obtained.

$$\frac{\partial(\rho\mathbf{u})}{\partial t} + \nabla\cdot(\rho\mathbf{u}\mathbf{u}) = \nabla\cdot\left(\eta\left(\nabla\mathbf{u} + \nabla\mathbf{u}^T\right) - p\mathbf{I}\right) + \mathbf{f}. \tag{2.5}$$

2.2 Solid equation

For solid phase, the elastodynamic equation is used,

$$\frac{D(\rho\mathbf{u})}{Dt} = \nabla\cdot\boldsymbol{\sigma}_s + \mathbf{f}. \tag{2.6}$$

The solid stress tensor, $\boldsymbol{\sigma}_s$ is written as

$$\boldsymbol{\sigma}_s = 2\mu\boldsymbol{\varepsilon} + \left(\lambda\,\mathrm{Tr}(\boldsymbol{\varepsilon})\right)\mathbf{I}, \tag{2.7}$$

where Tr is trace, $\boldsymbol{\varepsilon}$ is the strain tensor and μ and λ are Lame's constant as follows:

$$\boldsymbol{\varepsilon} = \frac{1}{2}\left(\nabla\mathbf{d} + \nabla\mathbf{d}^T\right), \tag{2.8}$$

$$\mu = \frac{E}{2(1+\nu)} \quad \text{and} \quad \lambda = \frac{E\nu}{(1+\nu)(1-2\nu)}. \tag{2.9}$$

Here, $\mathbf{d}$ is displacement vector, E is Young's modulus, and ν is Poisson's ratio.

From Eqs. (2.6), (2.7), and (2.8), the following momentum equation for solids is obtained.

$$\frac{\partial(\rho\mathbf{u})}{\partial t}+\nabla\cdot(\rho\mathbf{u}\mathbf{u})=\nabla\cdot\left(\mu\left(\nabla\mathbf{d}+\nabla\mathbf{d}^T\right)+\lambda(\nabla\cdot\mathbf{d})\mathbf{I}\right)+\mathbf{f}. \tag{2.10}$$

In this study, stationary boundary problems are considered where the displacement in Eq. (2.10) can be easily expressed in terms of velocity. For each computational cell, the displacement is obtained by integrating the velocity over time where the first-order implicit formulation is used as follows:

$$\mathbf{d}=\int_{t_o}^{t}\mathbf{u}dt+\mathbf{d}^o\approx\mathbf{u}\Delta t+\mathbf{d}^o. \tag{2.11}$$

The superscript o in Eq. (2.11) denotes the previous time step. Substituting Eq. (2.11) into Eq. (2.10), a velocity based formulation of the solid momentum equation can be obtained as

$$\frac{\partial(\rho\mathbf{u})}{\partial t}+\nabla\cdot(\rho\mathbf{u}\mathbf{u})=\nabla\cdot\left(\mu\Delta t\left(\nabla\mathbf{u}+\nabla\mathbf{u}^T\right)+\lambda\Delta t(\nabla\cdot\mathbf{u})\mathbf{I}+\mathbf{b}\right)+\mathbf{f}, \tag{2.12}$$

where $\mathbf{b}$ is written in terms of the displacement from previous time step.

$$\mathbf{b}=\mu\left(\nabla\mathbf{d}^o+\nabla\mathbf{d}^{oT}\right)+\lambda(\nabla\cdot\mathbf{d}^o)\mathbf{I}. \tag{2.13}$$

2.3 Unified momentum equation

Observing Eqs. (2.5) and (2.12) closely, we can notice that they are very similar. If $\bar{\mu}$ and $\bar{\lambda}$ are defined as

$$\bar{\mu}=\begin{cases}\eta & \text{for fluids,}\\ \mu\Delta t & \text{for solids,}\end{cases}\quad\text{and}\quad\bar{\lambda}=\begin{cases}0 & \text{for fluids,}\\ \lambda\Delta t & \text{for solids,}\end{cases} \tag{2.14}$$

the following unified momentum equation can be obtained from Eqs. (2.5) and (2.12):

$$\frac{\partial(\rho\mathbf{u})}{\partial t}+\nabla\cdot(\rho\mathbf{u}\mathbf{u})=\nabla\cdot\left(\bar{\mu}\left(\nabla\mathbf{u}+\nabla\mathbf{u}^T\right)+\bar{\lambda}(\nabla\cdot\mathbf{u})\mathbf{I}+\bar{\mathbf{b}}\right)+\mathbf{f}, \tag{2.15}$$

where $\bar{\mathbf{b}}$ is the source term which consists of the pressure or the displacement from previous time step according to the phase

$$\bar{\mathbf{b}}=\begin{cases}-p\mathbf{I} & \text{for fluids,}\\ \frac{\bar{\mu}}{\Delta t}\left(\nabla\mathbf{d}^o+\nabla\mathbf{d}^{oT}\right)+\frac{\bar{\lambda}}{\Delta t}(\nabla\cdot\mathbf{d}^o)\mathbf{I} & \text{for solids.}\end{cases} \tag{2.16}$$

However, this unified momentum equation is highly discontinuous since the properties such as density, $\bar{\mu}$ and $\bar{\lambda}$ change sharply at the fluid-structure interface.

In this study, in order to smooth out these discontinuities, the level set function ϕ is employed [30] where the level set function is defined as the signed normal distance from the interface.

$$\phi = \begin{cases} +\text{distance}, & \text{for fluids}, \\ 0, & \text{for interface}, \\ -\text{distance}, & \text{for solids}. \end{cases} \tag{2.17}$$

Using the level set function, the smoothed Heaviside function is defined as follows

$$h_\alpha(\phi) = \begin{cases} 1 & \text{if } \phi > \alpha, \\ \frac{1}{2}\left(1+\frac{\phi}{\alpha}+\frac{1}{\pi}\sin\left(\frac{\pi\phi}{\alpha}\right)\right) & \text{if } |\phi| \le \alpha, \\ 0 & \text{if } \phi < -\alpha. \end{cases} \tag{2.18}$$

Using this function, the interface has a finite thickness of 2α. Note that in the smeared interface region, velocity is more strongly affected by solid properties and velocity values are close to zero even in the fluid side of the smeared boundary. Therefore, if the smearing is done with respect to the zero level set, it is as though an additional solid layer of width α exists in the fluid side of the boundary. To figure out this issue, the entire smearing region is placed inside the solid region by using a shifted Heaviside function of $\mathrm{H}_\alpha(\phi) \equiv h_\alpha(\phi+\alpha)$ instead of the original one given in Eq. (2.18).

Across this region, the material properties and the $\bar{\mathbf{b}}$ term are smeared as follows:

$$\begin{aligned} &\rho = \rho_{\text{solid}} + (\rho_{\text{fluid}} - \rho_{\text{solid}})\mathrm{H}_\alpha(\phi), \\ &\bar{\mu} = \mu\Delta t + (\eta - \mu\Delta t)\mathrm{H}_\alpha(\phi), \\ &\bar{\lambda} = \lambda\Delta t(1-\mathrm{H}_\alpha(\phi)), \\ &\bar{\mathbf{b}} = \left\{\frac{\bar{\mu}}{\Delta t}\left(\nabla\mathbf{d}^o + \nabla\mathbf{d}^{oT}\right) + \frac{\bar{\lambda}}{\Delta t}(\nabla\cdot\mathbf{d}^o)\mathbf{I}\right\}(1-\mathrm{H}_\alpha(\phi)) + (-p\mathbf{I})\mathrm{H}_\alpha(\phi). \end{aligned} \tag{2.19}$$

In this study, $\alpha = 1.5\Delta x$ is used.

The following equation is the final form of the unified momentum equation where ρ, $\bar{\mu}$ and $\bar{\lambda}$ are defined in Eq. (2.19).

$$\begin{cases} \frac{\partial(\rho\mathbf{u})}{\partial t} + \nabla\cdot(\rho\mathbf{u}\mathbf{u}) = \nabla\cdot\left(\bar{\mu}\left(\nabla\mathbf{u}+\nabla\mathbf{u}^T\right) + \bar{\lambda}(\nabla\cdot\mathbf{u})\mathbf{I} + \bar{\mathbf{b}}\right) + \mathbf{f}, \\ \bar{\mathbf{b}} = \left\{\frac{\bar{\mu}}{\Delta t}\left(\nabla\mathbf{d}^o+\nabla\mathbf{d}^{oT}\right) + \frac{\bar{\lambda}}{\Delta t}(\nabla\cdot\mathbf{d}^o)\mathbf{I}\right\}(1-\mathrm{H}_\alpha(\phi)) + (-p\mathbf{I})\mathrm{H}_\alpha(\phi). \end{cases} \tag{2.20}$$

The unified momentum equation can be applied to the entire domain including the fluid-structure interface and the interfacial conditions such as the velocity continuity and the stress continuity are automatically satisfied. Using this approach, geometrical nonlinearities can be automatically taken into account, too.

One thing to note is that the velocity field in the fluid phase has the constraint of the continuity equation. However, the velocity field from Eq. (2.20) involves both fluid and solid velocities. The detailed algorithm will be explained in the following section.

2.4 Numerical algorithm

In the present study, the unified momentum equation is discretized using a finite volume approach on a uniform staggered grid. As an example, the x-component of the unified momentum equation will be considered in two dimensions. Integrating Eq. (2.20) over a control volume, the following equation is obtained (see Fig. 1).

$$\begin{aligned}
&\frac{\partial(\rho u)}{\partial t}_{i+1/2,j}\Delta V_{i+1/2,j}\\
&=\left\{(-\rho uu)_{i+1,j}+\left(2\bar{\mu}_{i+1,j}+\bar{\lambda}_{i+1,j}\right)\left(\frac{\partial u}{\partial x}\right)_{i+1,j}+\bar{\lambda}_{i+1,j}\left(\frac{\partial v}{\partial y}\right)_{i+1,j}+\bar{b}_{i+1,j}\right\}\Delta A_{i+1,j}\\
&\quad-\left\{(-\rho uu)_{i,j}+\left(2\bar{\mu}_{i,j}+\bar{\lambda}_{i,j}\right)\left(\frac{\partial u}{\partial x}\right)_{i,j}+\bar{\lambda}_{i,j}\left(\frac{\partial v}{\partial y}\right)_{i,j}+\bar{b}_{i,j}\right\}\Delta A_{i,j}\\
&\quad+\left\{(-\rho vu)_{i+1/2,j+1/2}+\bar{\mu}_{i+1/2,j+1/2}\left(\frac{\partial u}{\partial y}+\frac{\partial v}{\partial x}\right)_{i+1/2,j+1/2}+\bar{b}_{i+1/2,j+1/2}\right\}\Delta A_{i+1/2,j+1/2}\\
&\quad-\left\{(-\rho vu)_{i+1/2,j-1/2}+\bar{\mu}_{i+1/2,j-1/2}\left(\frac{\partial u}{\partial y}+\frac{\partial v}{\partial x}\right)_{i+1/2,j-1/2}+\bar{b}_{i+1/2,j-1/2}\right\}\Delta A_{i+1/2,j-1/2}+f_x
\end{aligned} \tag{2.21}$$

where ΔV is the volume of a cell, and ΔA is the cell face area.

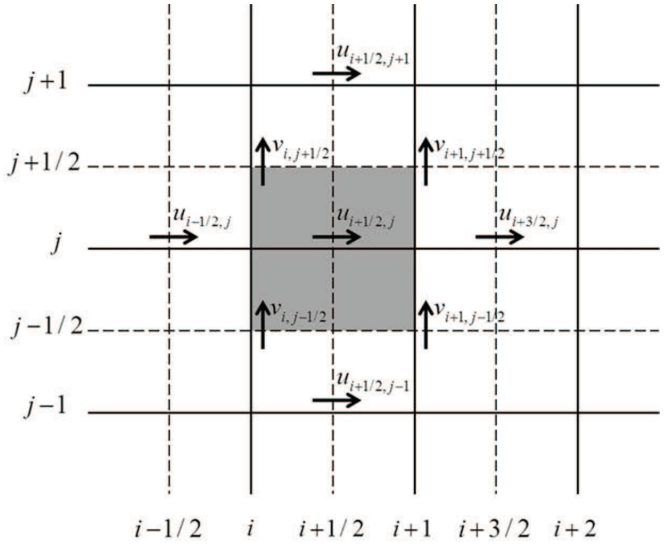

Figure 1: The schematic of the uniform staggered grid where a control volume for u-velocity is denoted as a shaded region.

Eq. (2.21) can be easily discretized. In this paper, the second-order central difference scheme for space and the first-order backward Euler scheme for time are used, and the

following discretized equation is obtained:

$$\begin{aligned}
&\frac{(\rho u)_{i+1/2,j}-(\rho u)^{o}_{i+1/2,j}}{\Delta t}\Delta V_{i+1/2,j}\\
&=\left\{(-\rho uu)_{i+1,j}+\left(2\bar{\mu}_{i+1,j}+\bar{\lambda}_{i+1,j}\right)\left(\frac{u_{i+3/2,j}-u_{i+1/2,j}}{\Delta x}\right)+\bar{\lambda}_{i+1,j}\left(\frac{v_{i+1,j+1/2}-v_{i+1,j-1/2}}{\Delta y}\right)\right.\\
&\left.+\bar{b}_{i+1,j}\right\}\Delta A_{i+1,j}-\left\{(-\rho uu)_{i,j}+\left(2\bar{\mu}_{i,j}+\bar{\lambda}_{i,j}\right)\left(\frac{u_{i+1/2,j}-u_{i-1/2,j}}{\Delta x}\right)+\bar{\lambda}_{i,j}\left(\frac{v_{i,j+1/2}-v_{i,j-1/2}}{\Delta y}\right)\right.\\
&\left.+\bar{b}_{i,j}\right\}\Delta A_{i,j}+\left\{(-\rho vu)_{i+1/2,j+1/2}+\bar{\mu}_{i+1/2,j+1/2}\left(\frac{u_{i+1/2,j+1}-u_{i+1/2,j}}{\Delta y}+\frac{v_{i+1,j+1/2}-v_{i,j+1/2}}{\Delta x}\right)\right.\\
&\left.+\bar{b}_{i+1/2,j+1/2}\right\}\Delta A_{i+1/2,j+1/2}-\left\{(-\rho vu)_{i+1/2,j-1/2}+\bar{\mu}_{i+1/2,j-1/2}\left(\frac{u_{i+1/2,j}-u_{i+1/2,j-1}}{\Delta y}\right.\right.\\
&\left.\left.+\frac{v_{i+1,j-1/2}-v_{i,j-1/2}}{\Delta x}\right)+\bar{b}_{i+1/2,j-1/2}\right\}\Delta A_{i+1/2,j-1/2}+f_x. \qquad (2.22)
\end{aligned}$$

Then, Eq. (2.22) can be written in the following form.

$$a_{i+1/2,j}u_{i+1/2,j}=\sum_{nb}a_{nb}u_{nb}+\left(p_{i,j}\mathrm{H}_\alpha\left(\phi_{i,j}\right)-p_{i+1,j}\mathrm{H}_\alpha\left(\phi_{i+1,j}\right)\right)\Delta A_{i+1/2,j}+S_{i+1/2,j}. \qquad (2.23)$$

Here, the subscript nb denotes the neighboring nodes and S is the source term. Similarly, the discretized momentum equation in the y-direction can be obtained as follows:

$$a_{i,j+1/2}v_{i,j+1/2}=\sum_{nb}a_{nb}v_{nb}+\left(p_{i,j}\mathrm{H}_\alpha\left(\phi_{i,j}\right)-p_{i,j+1}\mathrm{H}_\alpha\left(\phi_{i,j+1}\right)\right)\Delta A_{i,j+1/2}+S_{i,j+1/2}. \qquad (2.24)$$

Finally, the continuity equation (Eq. (2.2)) is discretized as follows:

$$(u\Delta A)_{i+1/2,j}-(u\Delta A)_{i-1/2,j}+(v\Delta A)_{i,j+1/2}-(v\Delta A)_{i,j-1/2}=0. \qquad (2.25)$$

In this study, the Semi-Implicit Method for Pressure Linked Equations (SIMPLE) algorithm [31] is employed as the coupling method. Note that the continuity equation (Eq. (2.25)) is only valid for the fluid phase and the pressure in Eqs. (2.23) and (2.24) is not defined in the solid phase. In this study, therefore, the pressure correction equation is obtained from the coupling of Eqs. (2.23)-(2.25) only for the fluid region and the smeared interface region, and is evaluated using the fluid properties (i.e., $\rho=\rho_{\text{fluid}}$, $\bar{\mu}=\eta$, $\bar{\lambda}=0$, and $\mathrm{H}_\alpha(\phi)=1$).

Following the SIMPLE procedure, the pressure correction equation is obtained as

$$a_{i,j}p'_{i,j}=a_{i+1,j}p'_{i+1,j}+a_{i-1,j}p'_{i-1,j}+a_{i,j+1}p'_{i,j+1}+a_{i,j-1}p'_{i,j-1}+b_{i,j}, \qquad (2.26)$$

where

$$\begin{aligned}
&a_{i+1,j}=\frac{\left(\Delta A_{i+1/2,j}\right)^2}{\left(a_{i+1/2,j}\right)_f},\ a_{i-1,j}=\frac{\left(\Delta A_{i-1/2,j}\right)^2}{\left(a_{i-1/2,j}\right)_f},\ a_{i,j+1}=\frac{\left(\Delta A_{i,j+1/2}\right)^2}{\left(a_{i,j+1/2}\right)_f},\ a_{i,j-1}=\frac{\left(\Delta A_{i,j-1/2}\right)^{1/2}}{\left(a_{i,j-1/2}\right)_f},\\
&a_{i,j}=a_{i+1,j}+a_{i-1,j}+a_{i,j+1}+a_{i,j-1},\\
&b_{i,j}=u^*_{i-1/2,j}\Delta A_{i-1/2,j}-u^*_{i+1/2,j}\Delta A_{i+1/2,j}+v^*_{i,j-1/2}\Delta A_{i,j-1/2}-v^*_{i,j+1/2}\Delta A_{i,j+1/2} \qquad (2.27)
\end{aligned}$$

and the subscript f indicates that the term is evaluated using the fluid properties.

Once pressure corrections are obtained from Eq. (2.26), the corrected pressure field is calculated:

$$p = p^* + p'. \tag{2.28}$$

Finally, the velocity field is updated using the original coefficients, $a_{i+1/2,j}$ and $a_{i,j+1/2}$ as follows:

$$u_{i+1/2,j} = u^*_{i+1/2,j} + \frac{\Delta A_{i+1/2,j}}{a_{i+1/2,j}} \left\{ p'_{i,j} \mathrm{H}_\alpha \left(\phi_{i,j}\right) - p'_{i+1,j} \mathrm{H}_\alpha \left(\phi_{i+1,j}\right) \right\}, \tag{2.29}$$

$$v_{i,j+1/2} = v^*_{i,j+1/2} + \frac{\Delta A_{i,j+1/2}}{a_{i,j+1/2}} \left\{ p'_{i,j} \mathrm{H}_\alpha \left(\phi_{i,j}\right) - p'_{i,j+1} \mathrm{H}_\alpha \left(\phi_{i,j+1}\right) \right\}. \tag{2.30}$$

The overall algorithm is shown in Fig. 2.

3 Numerical examples

In this section, three test examples are simulated on a uniform Cartesian grid with the presented method. In the first and second examples, lid-driven cavity flow problems inside two types of solid containers are considered: the first container has a square cavity, and the second container has a semi-circular cavity. The third example is the flow over a circular cylinder, where a stress field inside the cylinder is also considered. Using the unified momentum equation approach, velocity and stress fields are computed for both fluids and solids simultaneously. The simulation results are compared with the results from COMSOL Multiphysics®, where a partitioned approach on a body-fitted grid is used to handle the interaction between fluids and structures. The COMSOL simulations are performed on an Intel® Core™ i7-4770 CPU (3.40 GHz) PC. Also, the velocity fields are compared with the data from the literature.

3.1 Lid-driven cavity flow inside a solid container (square cavity)

A 0.12 m $\times$ 0.12 m cavity is located inside a solid container that has dimensions of 0.2 m $\times$ 0.16 m. Because the container is rigid, the cavity has the fixed shape and the container-structure boundary is stationary. The fluid flow is driven by a lid moving at a constant velocity of 8.333×10^{-3} m/s. The solid container is roller supported at the outer boundary. Fig. 3 shows a schematic of the problem. The fluid is assumed as water, which has a density of 1000 kg/m^3 and a viscosity of 1×10^{-3} kg/m·s. The Reynolds number of the problem is 1000. The solid container is made of aluminum, which has a density of 2700 kg/m^3, Young's modulus of 6.9×10^{10} N/m^2, and Poisson's ratio of 0.33. This problem is tested on a 500×400 grid, with a time step of 0.005 s.

Figs. 4-6 present the temporal evolution of stress distributions for both fluid and structure until the steady-state is reached. The normal stresses in x- and y-directions are presented in Fig. 4 and Fig. 5, respectively. As shown in the figures, stresses are developed

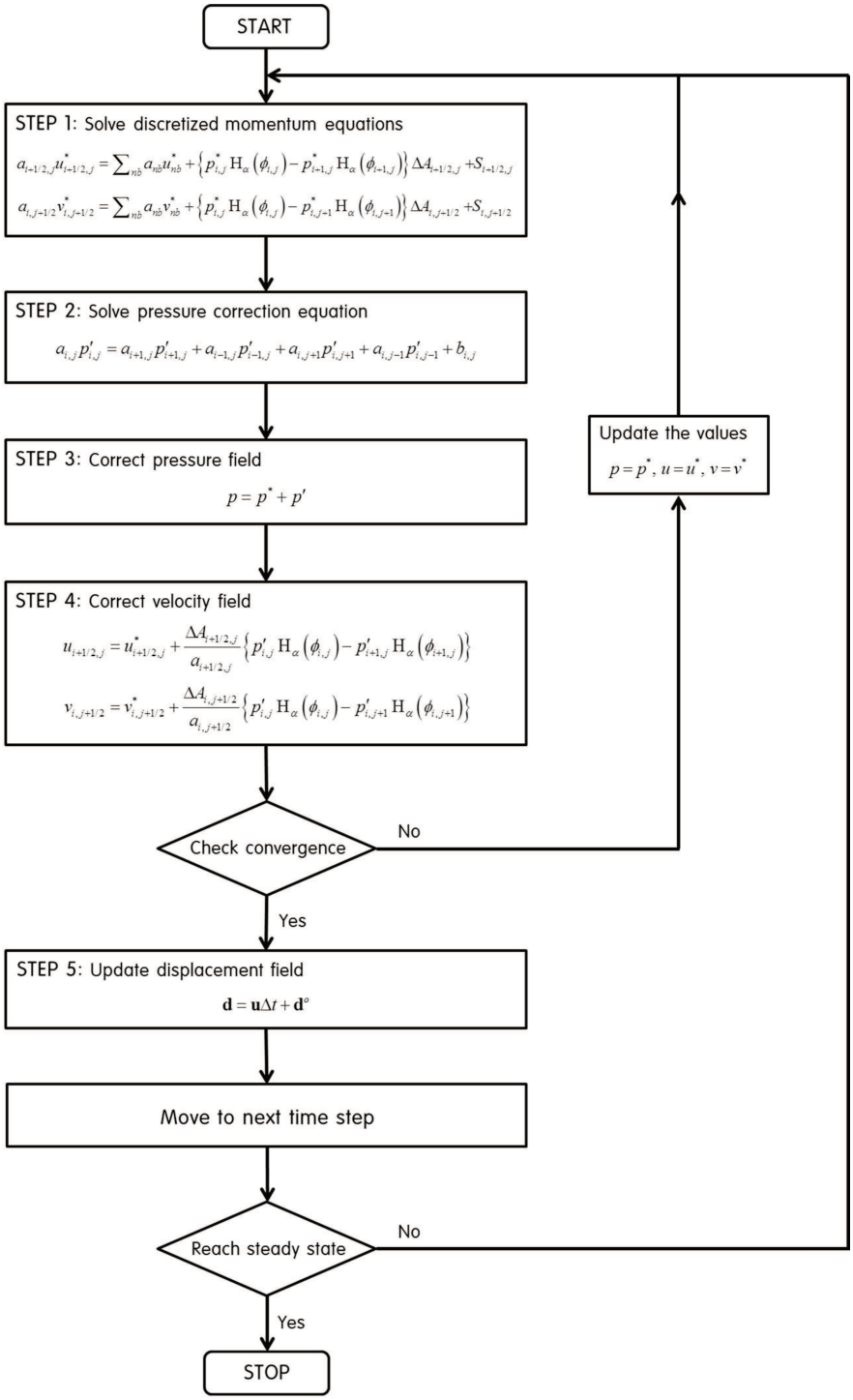

Figure 2: The SIMPLE algorithm applied to the unified momentum equation approach.

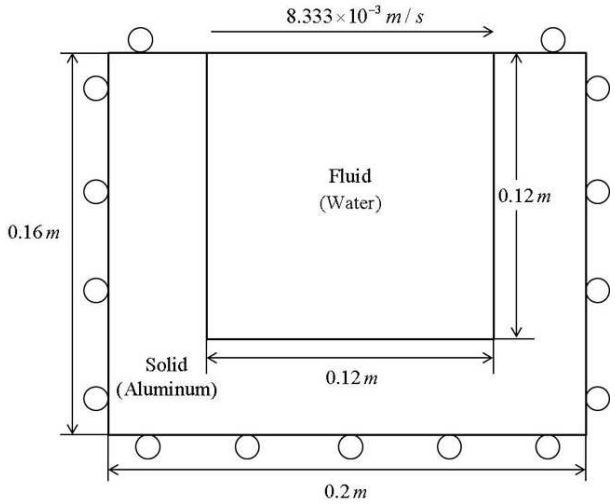

Figure 3: The schematic of the lid-driven rectangular cavity flow problem.

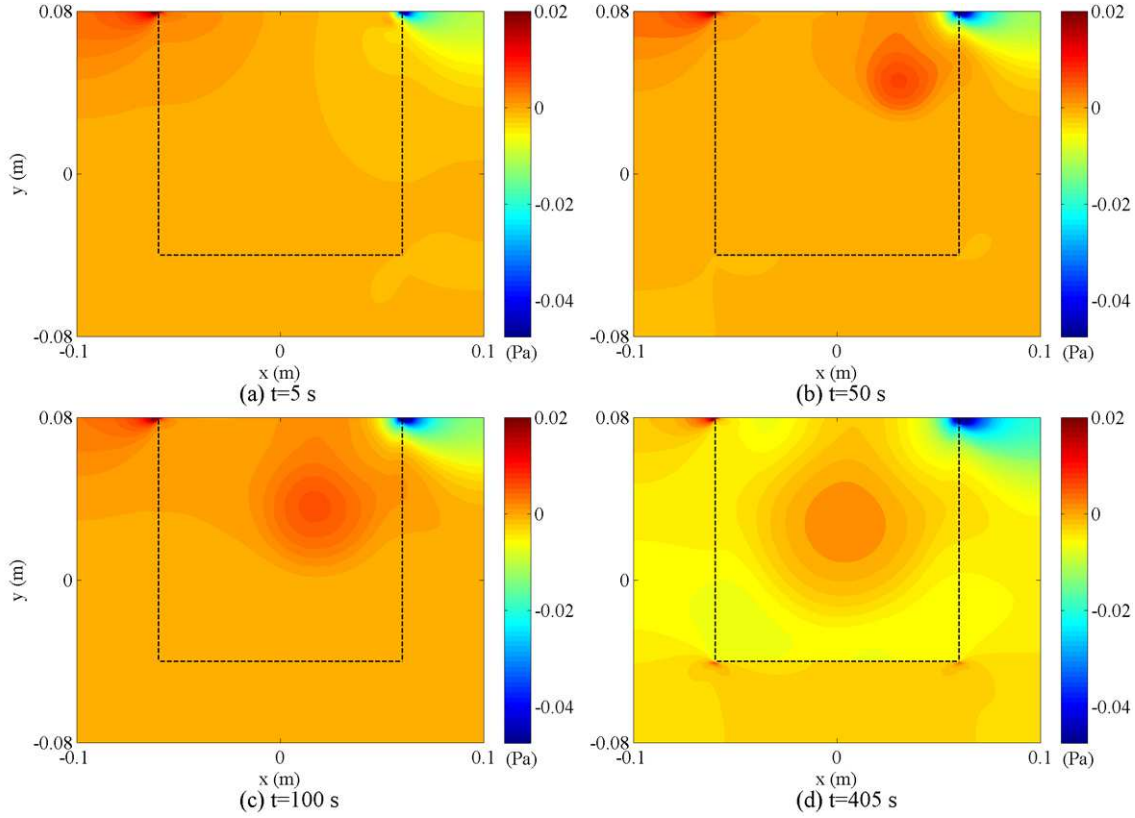

Figure 4: Evolution of normal stress (σ_{xx}): (a) $t=5$s; (b) $t=50$s; (c) $t=100$s and (d) $t=405$s (steady-state).

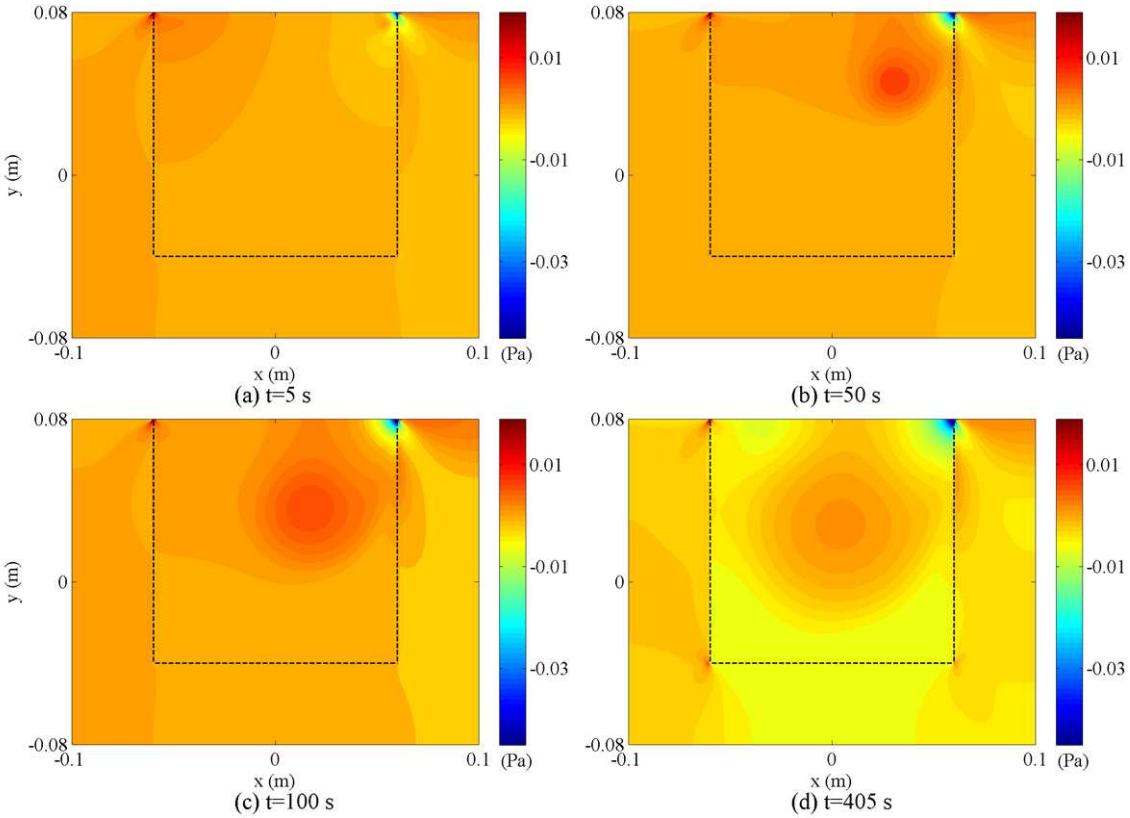

Figure 5: Evolution of normal stress (σ_{yy}): (a) $t=5$s; (b) $t=50$s; (c) $t=100$s and (d) $t=405$s (steady-state).

starting from the top right corner of the interface due to the flow direction. As time elapses, a circularly shaped stress distribution appears inside a fluid region, which indicates that a circular flow field is being developed there. From these figures, as expected, stress continuity is clearly observed at the interface. At the vertical interfaces, the normal stress in the x-direction (σ_{xx}) is continuous along the x-direction; at the horizontal interface, the normal stress in the y-direction (σ_{yy}) is also continuous along the y-direction. Fig. 6 presents shear stress distributions. Similarly to the normal stress distributions, shear stress is the largest at the top right corner of the interface, where the flow changes direction abruptly at the wall and a large shear stress is generated. Also, because the flow is generated by the moving lid at the top, shear stress is more noticeable right below the moving lid. From Figs. 4-6, we can observe that the stress field inside the solid container is getting fully established as time elapses, which confirms that flow-induced stresses are transferred to the structure well by the presented algorithm.

The streamline distributions for both phases are presented in Fig. 7. Note that although the velocities in the solid region are extremely small compared to the fluid velocities, it is still possible to define streamlines. In the fluid region, the development of

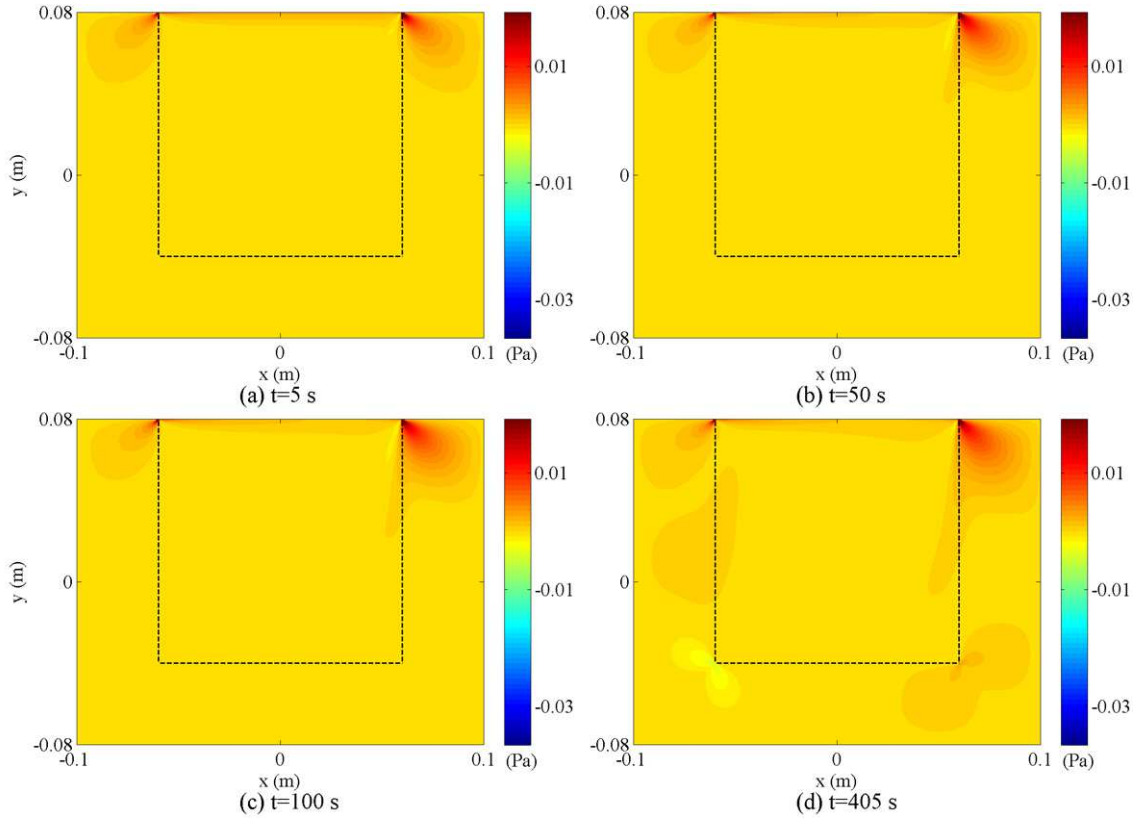

Figure 6: Evolution of shear stress (σ_{xy}): (a) $t=5$s; (b) $t=50$s; (c) $t=100$s and (d) $t=405$s (steady-state).

vortices is clearly observed. At first, the primary vortex is formed, and two secondary vortices are developed in the bottom-left and bottom-right corners of the interface. At the steady state (Fig. 7(d)), streamlines in the solid region have all disappeared, which means that the container is fully deformed due to the well-established flow field.

Fig. 8 shows a grid refinement study where the spatial error norms in the velocity field are plotted versus the number of x-direction grid points. Fig. 8(a) and (b) respectively show the x-directional and y-directional velocity results. For the analysis, 125×100, 250×200, and 500×400 uniform Cartesian grids were used, and the error norms in the velocity field were computed over the whole domain at steady state. As shown, the algorithm shows largely a second-order convergence.

In order to validate the accuracy of the algorithm, we simulated the same problem with COMSOL Multiphysics®. A total of 31440 triangular elements were used and it took about 19 minutes to reach the steady state with a maximum time step of 0.5 s. The steady-state stress field plots on the left side of Fig. 9 are obtained from COMSOL Multiphysics® simulations, which are qualitatively very similar to the corresponding figures in Figs. 4-6. For more quantitative comparison, the stress distributions along the two horizontal lines

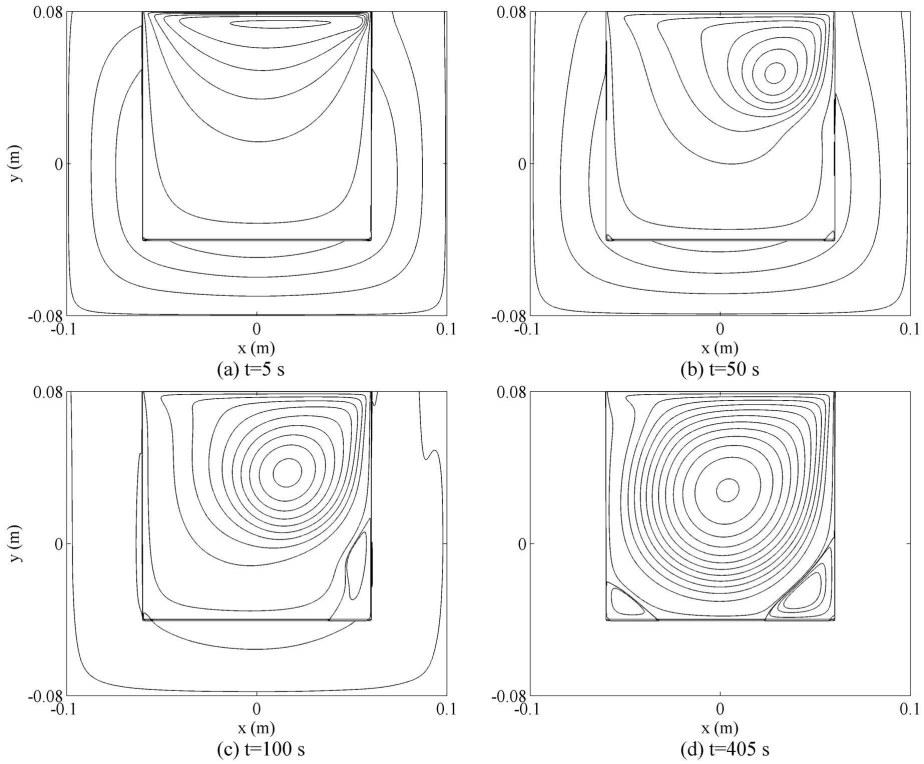

Figure 7: Evolution of streamlines: (a) $t=5$s; (b) $t=50$s; (c) $t=100$s and (d) $t=405$s (steady-state).

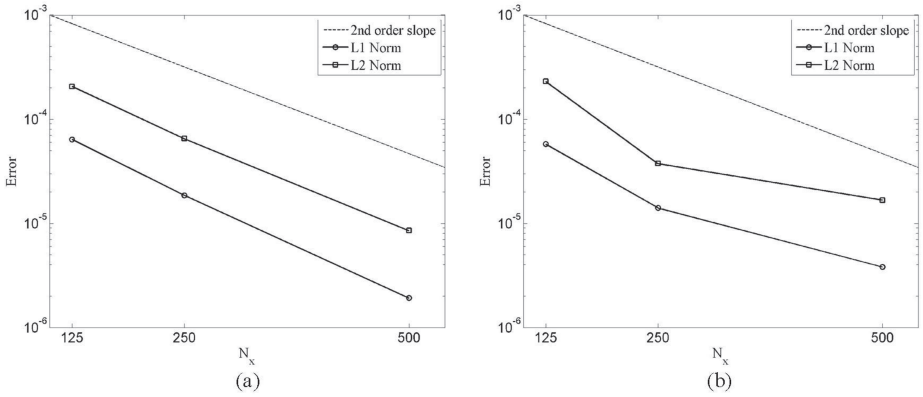

Figure 8: Grid convergence study result: (a) x-directional velocity, (b) y-directional velocity.

(the locations shown as dashed and solid lines in the left figures) are computed using the two methods and compared in the right figures, where the interface locations are shown as vertical lines. The current simulation results are in good agreement with the COMSOL Multiphysics® results although the interface is smeared using the level set function in the presented method. Fig. 10 shows the velocity field inside the cavity compared with the

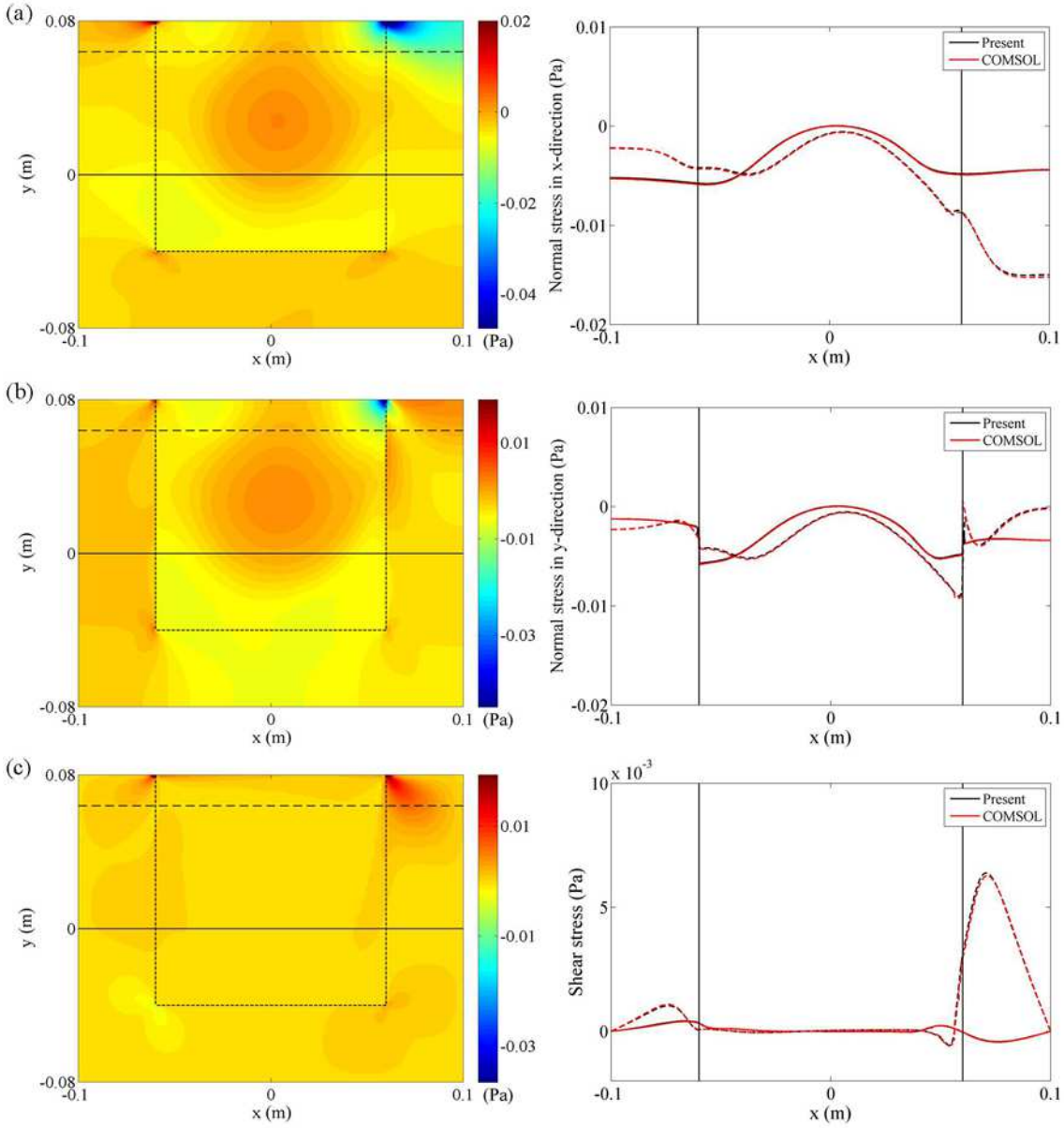

Figure 9: [Left figures] Steady-state ($t=405$s) stress fields obtained by COMSOL Multiphysics® with 31440 triangular elements and a maximum time step of 0.5 s. [Right figures] Comparison between the present study and COMSOL along the solid ($y=0$m) and dashed ($y=0.064$m) horizontal lines shown in the left figures. [From top to bottom] (a) Normal stress in the x-direction, (b) normal stress in the y-direction and (c) shear stress.

data available in reference [32]. Fig. 10(a) and (b) respectively show the x velocity profile along the middle vertical line of the cavity and the y velocity profile along the middle horizontal line of the cavity. As shown, a good agreement is observed.

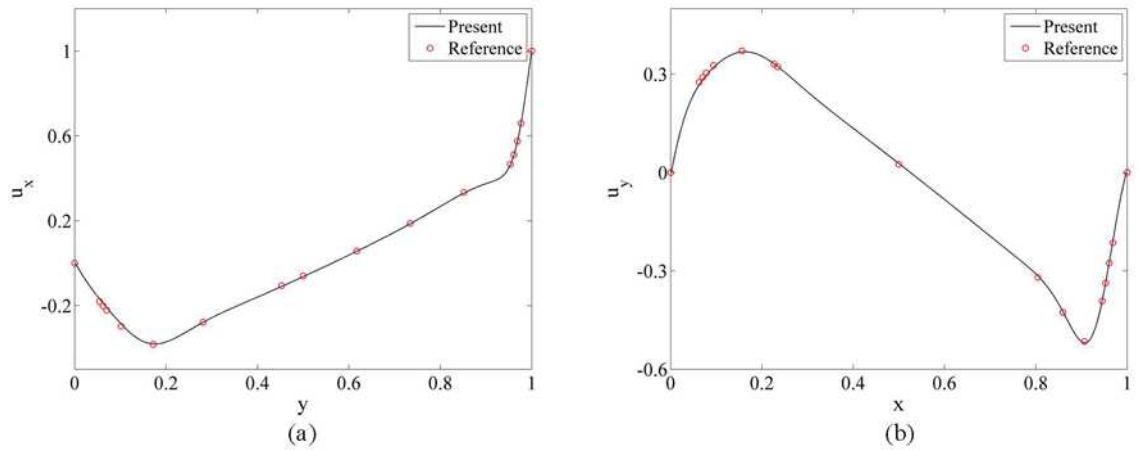

Figure 10: Comparison of fluid velocity profiles with the data in Ref. [32]. (a) x-directional fluid velocity along the middle vertical line of the cavity, (b) y-directional fluid velocity along the middle horizontal line of the cavity.

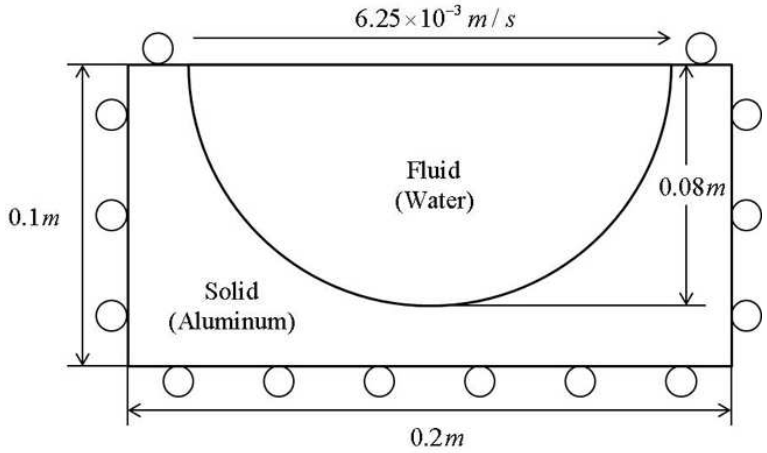

Figure 11: The schematic of the lid-driven semi-circular cavity flow problem.

3.2 Lid-driven cavity flow inside a solid container (semi-circular cavity)

A solid container with dimensions of 0.2 m $\times$ 0.1 m has a semi-circular cavity with a radius of 0.08 m. In this problem, different from the previous example, the fluid-structure interface is not aligned with the grid lines. Just like the previous problem, the cavity is filled with water and the solid container is made of aluminum. The flow is driven by a lid at the top that moves at a velocity of 6.25×10^{-3}m/s, and the solid container is roller supported at the outer boundary. The Reynolds number of the problem is 1000. Fig. 11 shows a schematic of the problem. This simulation is performed using a 512×256 grid, with a time step of 0.005 s.

The stress fields for the whole domain are shown at four different times in Figs. 12-14,

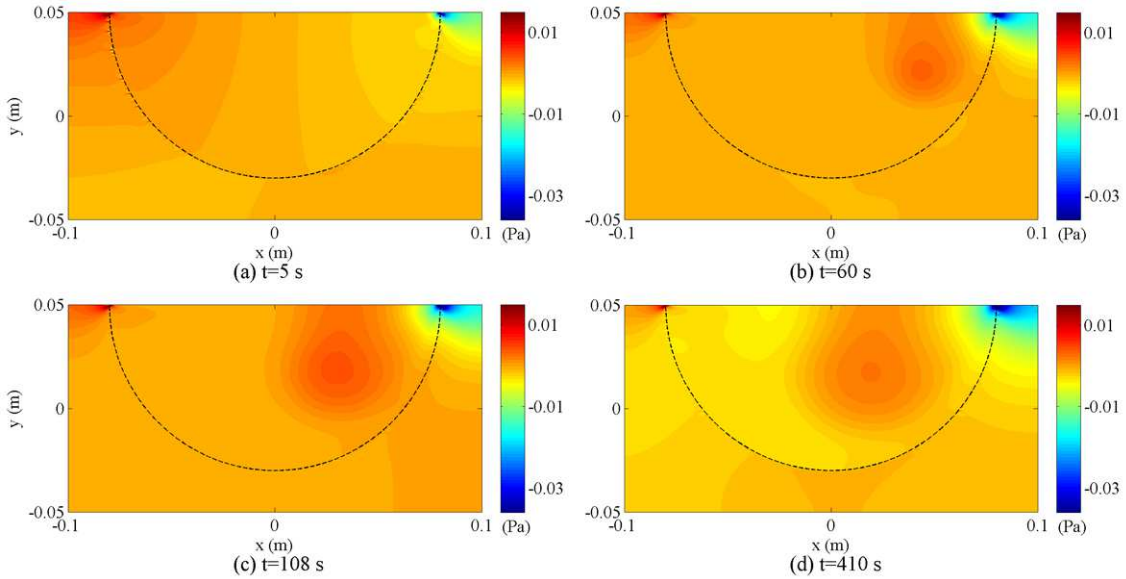

Figure 12: Evolution of normal stress (σ_{xx}): (a) $t=5$s; (b) $t=60$s; (c) $t=108$s and (d) $t=410$s (steady-state).

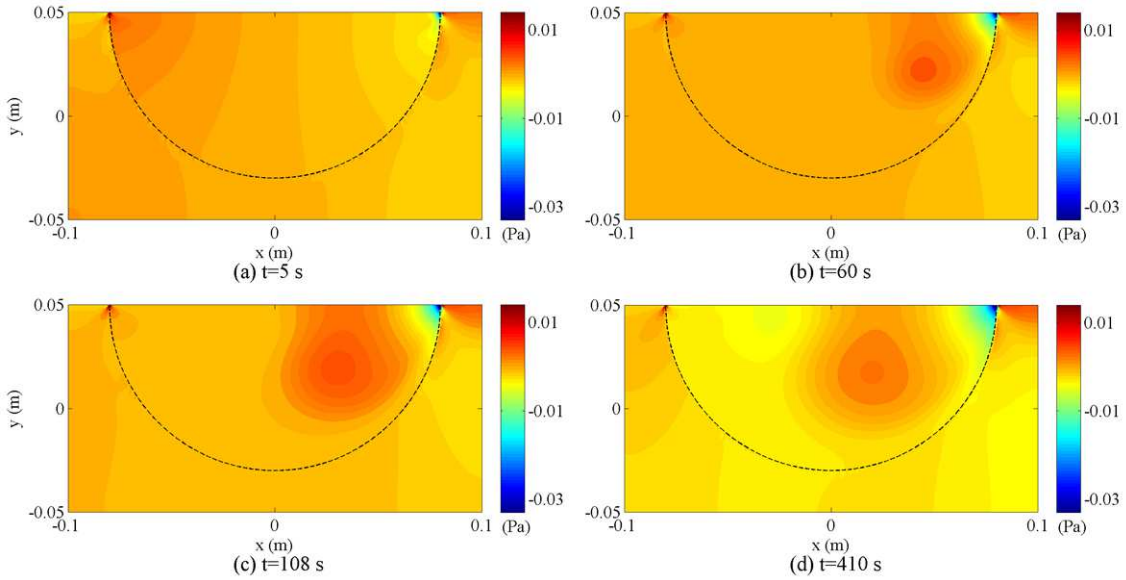

Figure 13: Evolution of normal stress (σ_{yy}): (a) $t=5$s; (b) $t=60$s; (c) $t=108$s and (d) $t=410$s (steady-state).

with the last ones being the steady-state results. The results exhibit the similar behavior as the previous example. As shown in the figures, the results look reasonably good with this curved interface, and the obtained stress fields are as predicted. The flow induced stresses are developed in the structure as time progresses (which shows that the stress

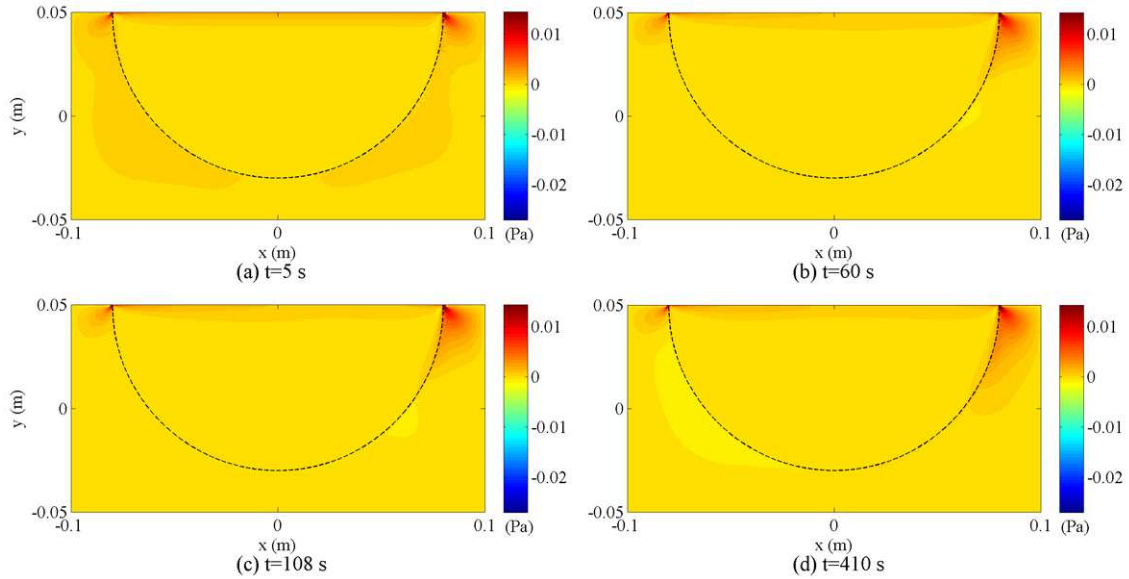

Figure 14: Evolution of shear stress (σ_{xy}): (a) $t=5$s; (b) $t=60$s; (c) $t=108$s and (d) $t=410$s (steady-state).

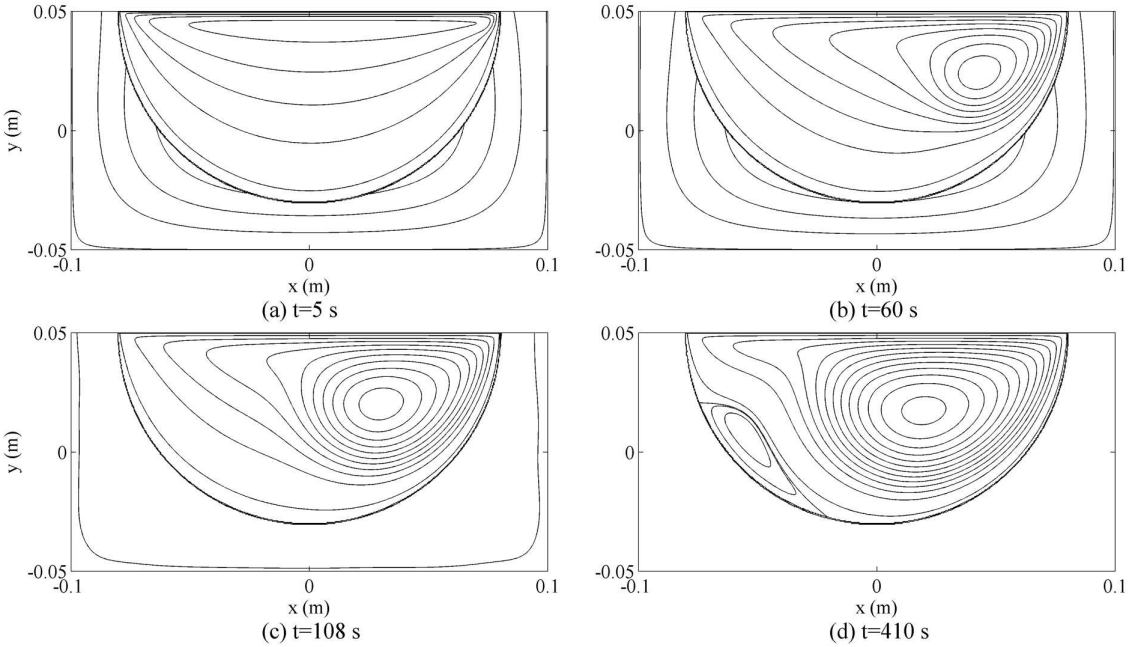

Figure 15: Evolution of streamlines: (a) $t=5$s; (b) $t=60$s; (c) $t=108$s and (d) $t=410$s (steady-state).

is well transferred to the structure in the numerical algorithm), and the stress is highly concentrated in the top-right corner of the interface. Because the fluid-structure interface is not aligned with the grid lines, stress continuity is less obvious in the figures. In this

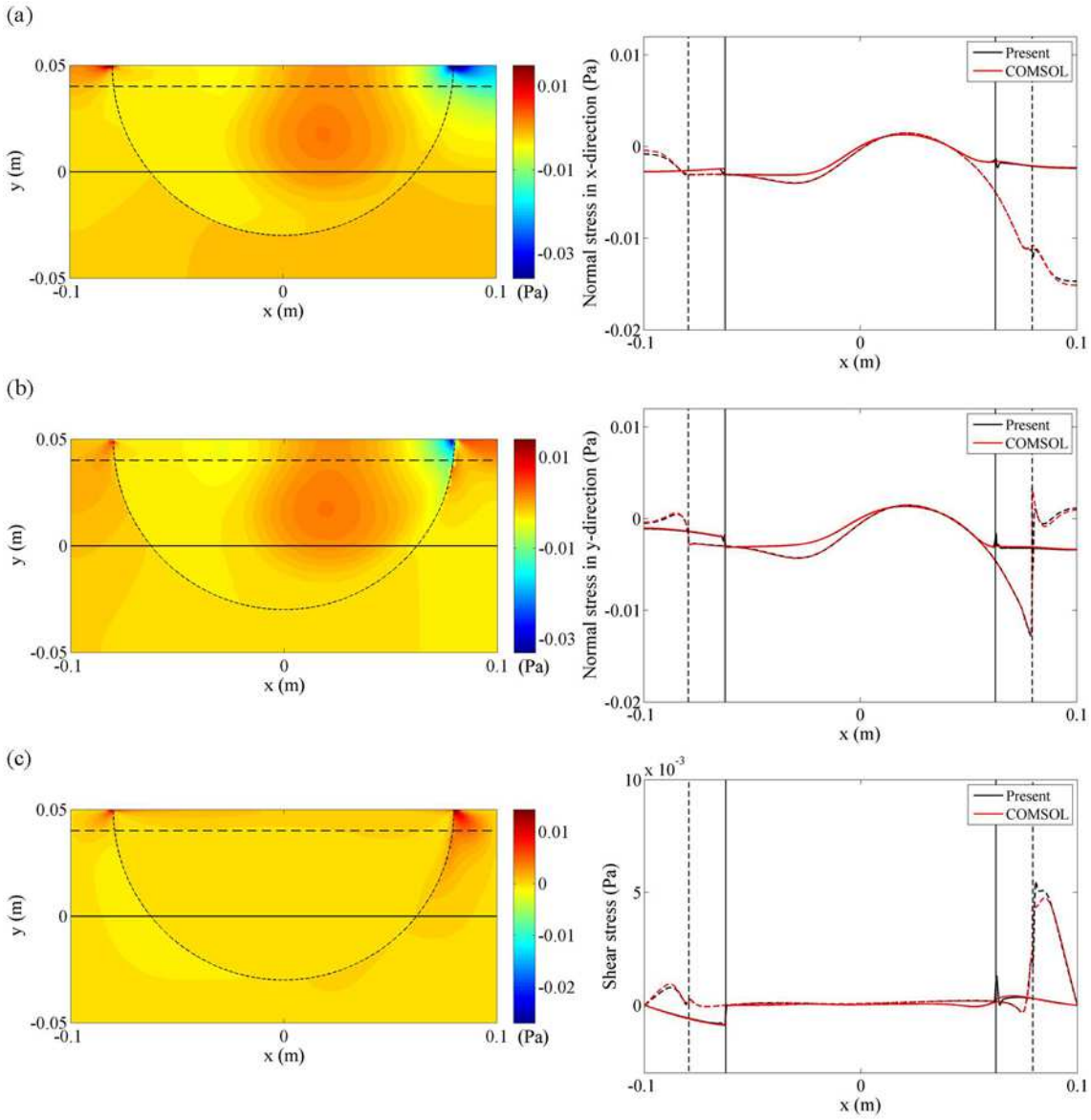

Figure 16: [Left figures] Steady-state (t=410s) stress fields obtained by COMSOL Multiphysics® with 40245 triangular elements and a maximum time step of 0.5 s. [Right figures] Comparison between the present study and the COMSOL simulation along the solid (y=0m) and dashed (y=0.04m) horizontal lines shown in the left figures. [From top to bottom] (a) Normal stress in the x-direction, (b) normal stress in the y-direction and (c) shear stress.

case, the normal stress in the x-direction (σ_{xx}) is continuous along the x-direction at the top-right and top-left interface and the normal stress in the y-direction (σ_{yy}) is continuous along the y-direction at the bottom interface. Also, the stress fields indicate that there is

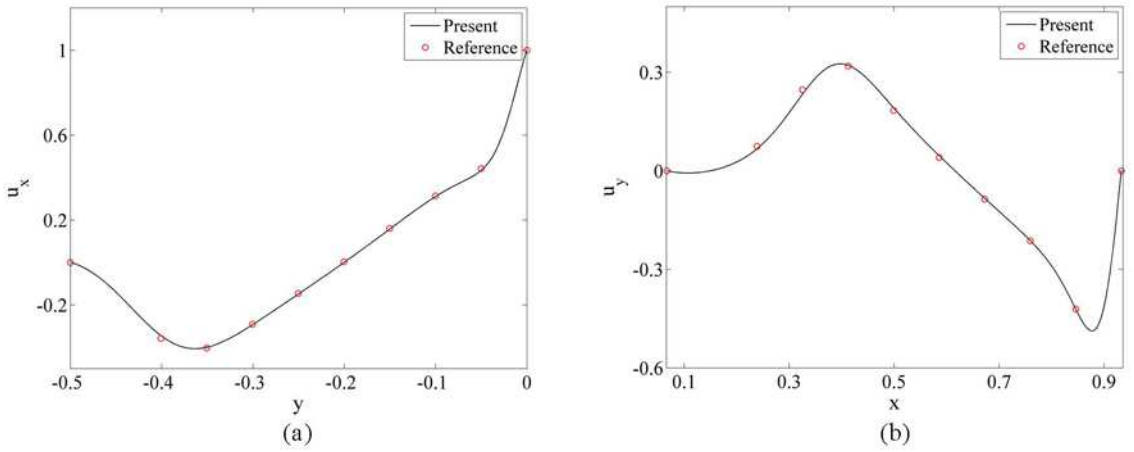

Figure 17: Comparison of fluid velocity profiles with the data in Ref [33]. (a) x-directional fluid velocity along the middle vertical line of the cavity, (b) y-directional fluid velocity along the horizontal line which is one fourth of the cavity depth below from the surface.

circularly shaped flow structure inside the flow region, which is more clearly seen in the streamline plots in Fig. 15. As shown in Fig. 15, while the deformation is progressing in the solid domain, well-shaped streamlines exist even for solids, which all disappear completely when the fluid-induced deformation is finalized.

For validation purposes, the same problem was simulated using COMSOL Multiphysics®. A total of 40245 triangular elements were used and it took 23 minutes to reach the steady state with a maximum time step of 0.5 s, and the obtained steady-state stress fields are presented in the left side of Fig. 16. The stress fields from both simulations are reasonably similar, as the stress distributions along the reference lines are compared in the right side of Fig. 16. Although some spikes are observed in the smeared interface region, the current simulation results are in good agreement with the COMSOL Multiphysics® results even for the curved boundary problems. Note that COMSOL Multiphysics® are based on a partitioned approach and the interfaces are aligned with the grid lines. Fig. 17 shows the velocity field inside the cavity compared with the data available in reference [33]. Fig. 17 (a) and (b) respectively show the x-directional fluid velocity along the middle vertical line of the cavity and the y-directional fluid velocity along the horizontal line which is one fourth of the cavity depth below from the surface. As shown, a good agreement is observed.

3.3 Flow over a circular cylinder

As the last example, the flow past a circular cylinder is considered, where the stress field inside the cylinder that is also made of aluminum, is solved simultaneously with the flow field in terms of velocity. A circular cylinder with a diameter (D) of 0.3 m is placed at $x=-8$D, $y=0$ when the computational domain has a size of 32 D $\times$ 16 D ($-16\text{D}\leq x\leq 16\text{D}$,

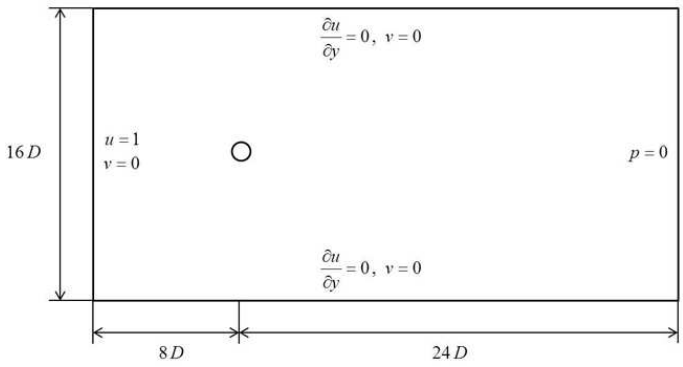

Figure 18: Computational domain and boundary conditions for the flow-over-a-cylinder problem.

$-8\text{D}\leq y\leq 8\text{D}$). A fluid with a density of 1kg/m^3 and a viscosity is $3\times10^{-3}\text{kg/m·s}$ flows from left at $U_\infty=1\text{m/s}$, and the solid cylinder is fixed at two points, $x=-8\text{D}$, $y=\pm0.34\text{D}$. The schematic of the problem is shown in Fig. 18, together with the boundary conditions. The Reynolds number of the flow is 100. This simulation is performed on a 512×256 grid, with a time step of 0.005 s.

Fig. 19 shows the normal stresses and vorticity distributions at $t=113\text{s}$. In order to resist the drag force due to the flow, stress is concentrated at the two fixed points inside the cylinder, and as the vorticity distribution shows, the von Karman vortex street is formed behind the cylinder. Fig. 20 presents the magnified views of normal stress fields around the cylinder, and the normal stress distributions along the horizontal central line are compared with COMSOL simulation results in Fig. 21, where two vertical lines indicate the boundaries of the cylinder. For COMSOL simulations, 64708 triangular elements were used and it took 63 minutes to simulate 113 s with a maximum time step of 0.1 s. As shown in the figure, the two results agree reasonably well with each other. Although the difference seems to be a bit larger than the previous two examples due to the relatively larger smeared interface region compared to the structure size, the two results are still reasonably close.

4 Conclusion

A novel monolithic method for calculating flow induced stresses in structures having arbitrarily-shaped stationary boundaries has been presented. In this study, a unified momentum equation that is valid for both fluids and solids is derived in terms of velocity, and the momentum equations for fluids and solids are hybridized around the interface using the level set function. The SIMPLE algorithm is employed to solve the governing equations numerically. This method has been successfully tested with three examples, and we believe that this method is simple to implement and can be easily applied to many other similar problems.

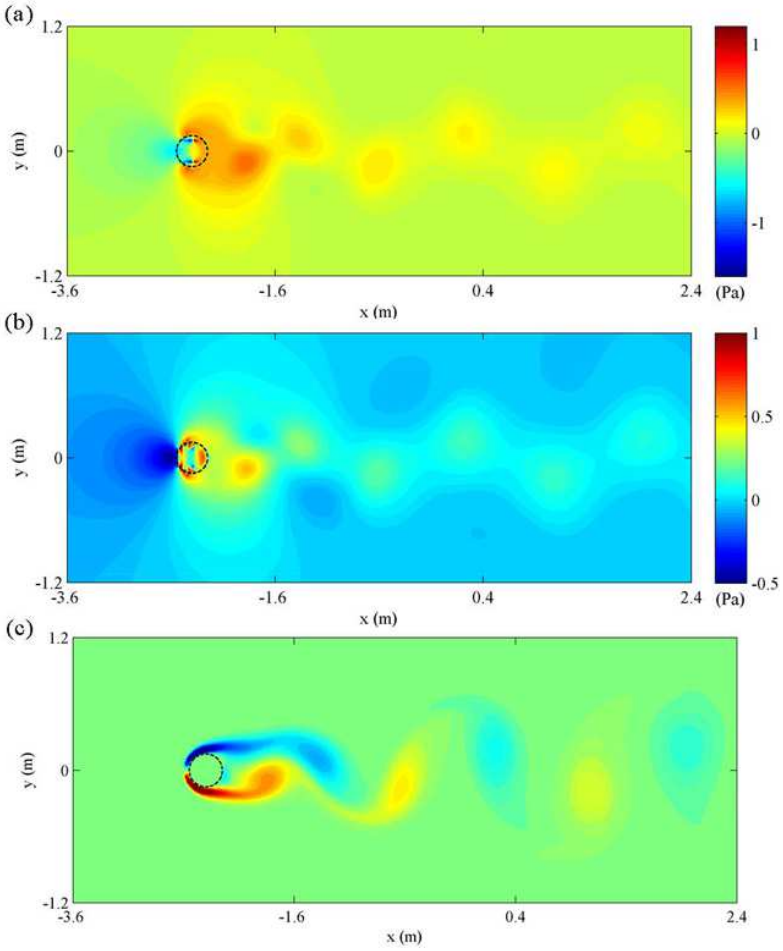

Figure 19: Simulation results of the flow over a circular cylinder at $t=113$s: (a) normal stress in the x-direction, (b) normal stress in the y-direction and (c) vorticity field.

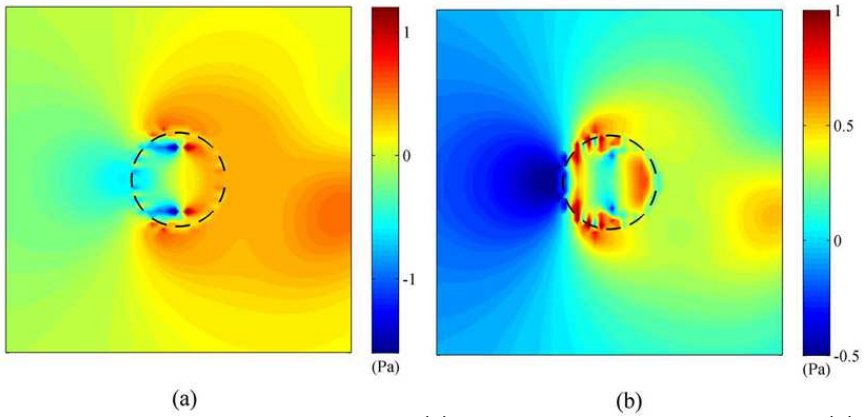

Figure 20: Stress fields magnified around the cylinder: (a) normal stress in the x-direction and (b) normal stress in the y-direction.

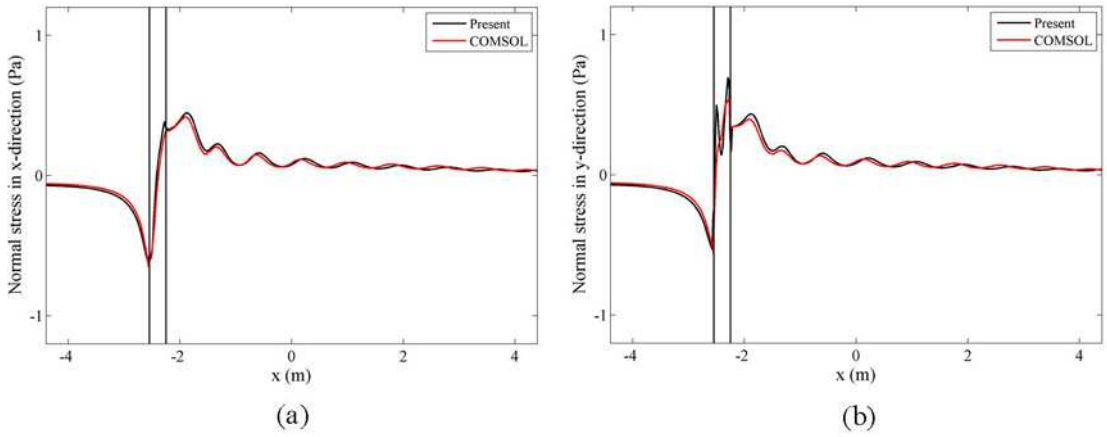

Figure 21: Comparison between the present study and the COMSOL simulation along the central horizontal line: (a) Normal stress in the x-direction, (b) normal stress in the y-direction.

Acknowledgments

This research was supported by the 2016 Research Fund (1.160005.01) of UNIST (Ulsan National Institute of Science and Technology), and was performed using a Linux cluster of the UNIST supercomputing center.

References

[1] Y. Bazilevs, M.-C. Hsu, Y. Zhang, W. Wang, X. Liang, T. Kvamsdal, R. Brekken, J.G. Isaksen, A fully-coupled fluid-structure interaction simulation of cerebral aneurysms, Computational Mechanics, 46 (2009) 3-16.

[2] D. Kamensky, M.C. Hsu, D. Schillinger, J.A. Evans, A. Aggarwal, Y. Bazilevs, M.S. Sacks, T.J.R. Hughes, An immersogeometric variational framework for fluid-structure interaction: Application to bioprosthetic heart valves, Computer Methods in Applied Mechanics and Engineering, 284 (2015) 1005-1053.

[3] M.-C. Hsu, I. Akkerman, Y. Bazilevs, Finite element simulation of wind turbine aerodynamics: Validation study using NREL Phase VI experiment, Wind Energy, 17 (2014) 461-481.

[4] K.-J. Paik, P.M. Carrica, D. Lee, K. Maki, Strongly coupled fluid-structure interaction method for structural loads on surface ships, Ocean Engineering, 36 (2009) 1346-1357.

[5] G. Hou, J. Wang, A. Layton, Numerical methods for fluid-structure interaction - A review, Communications in Computational Physics, 12 (2012) 337-377.

[6] C.A. Felippa, K.C. Park, C. Farhat, Partitioned analysis of coupled mechanical systems, Computer Methods in Applied Mechanics and Engineering, 190 (2001) 3247-3270.

[7] C. Farhat, K.G. van der Zee, P. Geuzaine, Provably second-order time-accurate loosely-coupled solution algorithms for transient nonlinear computational aeroelasticity, Computer Methods in Applied Mechanics and Engineering, 195 (2006) 1973-2001.

[8] P. Causin, J.F. Gerbeau, F. Nobile, Added-mass effect in the design of partitioned algorithms for fluid-structure problems, Computer Methods in Applied Mechanics and Engineering, 194 (2005) 4506-4527.
[9] H.G. Matthies, R. Niekamp, J. Steindorf, Algorithms for strong coupling procedures, Computer Methods in Applied Mechanics and Engineering, 195 (2006) 2028-2049.
[10] B. Hübner, E. Walhorn, D. Dinkler, A monolithic approach to fluid-structure interaction using space-time finite elements, Computer Methods in Applied Mechanics and Engineering, 193 (2004) 2087-2104.
[11] M. Heil, An efficient solver for the fully coupled solution of large-displacement fluid-structure interaction problems, Computer Methods in Applied Mechanics and Engineering, 193 (2004) 1-23.
[12] P.B. Ryzhakov, R. Rossi, S.R. Idelsohn, E. Oñate, A monolithic Lagrangian approach for fluid-structure interaction problems, Computational Mechanics, 46 (2010) 883-899.
[13] A. Franci, E. Oñate, J.M. Carbonell, Unified Lagrangian formulation for solid and fluid mechanics and FSI problems, Computer Methods in Applied Mechanics and Engineering, 298 (2016) 520-547.
[14] C.S. Peskin, Numerical analysis of blood flow in heart, Journal of Computational Physics, 25 (1977) 220-252.
[15] C.S. Peskin, The immersed boundary method, Acta Numerica, 11 (2002) 479-517.
[16] J. Mohd-Yusof, Combined immersed-boundary/B-spline methods for simulations of flow in complex geometries, in: Annual Research Briefs, Center for Turbulence Research, Stanford University, Stanford, (1997) 317-327.
[17] J. Yang, F. Stern, A simple and efficient direct forcing immersed boundary framework for fluid-structure interactions, Journal of Computational Physics, 231 (2012) 5029-5061.
[18] T. Ye, R. Mittal, H.S. Udaykumar, W. Shyy, An accurate Cartesian grid method for viscous incompressible flows with complex immersed boundaries, Journal of Computational Physics, 156 (1999) 209-240.
[19] L. Schneiders, D. Hartmann, M. Meinke, W. Schröder, An accurate moving boundary formulation in cut-cell methods, Journal of Computational Physics, 235 (2013) 786-809.
[20] Y.-H. Tseng, J.H. Ferziger, A ghost-cell immersed boundary method for flow in complex geometry, Journal of Computational Physics, 192 (2003) 593-623.
[21] J. Lee, D. You, An implicit ghost-cell immersed boundary method for simulations of moving body problems with control of spurious force oscillations, Journal of Computational Physics, 233 (2013) 295-314.
[22] L. Zhang, A. Gerstenberger, X. Wang, W.K. Liu, Immersed finite element method, Computer Methods in Applied Mechanics and Engineering, 193 (2004) 2051-2067.
[23] A.J. Gil, A. Arranz Carreño, J. Bonet, O. Hassan, An enhanced immersed structural potential method for fluid-structure interaction, Journal of Computational Physics, 250 (2013) 178-205.
[24] R. Glowinski, T.W. Pan, J. Periaux, A fictitious domain method for Dirichlet problem and applications, Computer Methods in Applied Mechanics and Engineering, 111 (1994) 283-303.
[25] F.P.T. Baaijens, A fictitious domain/mortar element method for fluid-structure interaction, International Journal for Numerical Methods in Fluids, 35 (2001) 743-761.
[26] Z. Yu, A DLM/FD method for fluid/flexible-body interactions, Journal of Computational Physics, 207 (2005) 1-27.
[27] M.R. Swift, E. Orlandini, W.R. Osborn, J.M. Yeomans, Lattice Boltzmann simulations of liquid-gas and binary fluid systems, Physical Review E, 54 (1996) 5041-5052.

[28] A.J.C. Ladd, Numerical simulations of particulate suspensions via a discretized Boltzmann equation. Part I. Theoretical foundation, Journal of Fluid Mechanics, 271 (1994) 285-309.
[29] A.J.C. Ladd, R. Verberg, Lattice-Boltzmann simulations of particle-fluid suspensions, Journal of Statistical Physics, 104 (2001) 1191-1251.
[30] M. Sussman, P. Smereka, S. Osher, A level set approach for computing solutions to incompressible two-phase flow, Journal of Computational Physics, 114 (1994) 146-159.
[31] S.V. Patankar, Numerical Heat Transfer and Fluid Flow, (1980) Hemisphere Publishing Corporation.
[32] U. Ghia, K.N. Ghia, C.T. Shin, High-Re solutions for incompressible flow using the Navier-Stokes equations and a multigrid method, Journal of Computational Physics, 48 (1982) 387-411.
[33] R. Glowinski, G. Guidoboni, T.W. Pan, Wall-driven incompressible viscous flow in a two-dimensional semi-circular cavity, Journal of Computational Physics, 216 (2006) 76-91.